Effects of hydrogen on the phase relations in Fe–FeS at pressures of Mars-sized bodies

Hélène Piet[1], Kurt Leinenweber[1], Eran Greenberg[2], Vitali B Prakapenka[3], and Sang-Heon Shim[1]

[1]Arizona State University
[2]Center for Advanced Radiation Sources, University of Chicago
[3]University of Chicago

November 22, 2022

Abstract

Hydrogen (H) and sulfur (S) are light element candidates to enter the core of planetary bodies. Although Fe-S and Fe-H systems have been studied individually, the Fe-S-H ternary system has only been investigated up to 16 GPa and 1723 K. We have investigated the Fe-S-H system at pressures and temperatures (P-T) relevant to the cores of Mars-sized planets (up to 45 GPa and well above the melting temperature of FeS) in the laser-heated diamond anvil cell combined with in situ synchrotron X-ray diffraction. We found that at high P-T, Fe3S is unstable if H exists in the system. Instead, separate Fe–H and Fe–S phases appear at 23–35 GPa. At pressures above 35 GPa, we found a new phase appearing while Fe–S phases disappear and Fe–H phases remain. Our analysis indicates that the new phase likely contains both S and H in the crystal structure (tentatively FeSH). The observed pressure dependent changes in the phase relation may be important for understanding the structure and dynamics of the Martian core and the cores of Mars-sized exoplanets.

Effects of hydrogen on the phase relations in Fe–FeS at pressures of Mars-sized bodies

H. Piet[1], K. Leinenweber[2], E. Greenberg[3], V. B. Prakapenka[3], and S.-H. Shim[1]

[1]School of Earth and Space Exploration, Arizona State University, Tempe, Arizona 85287, U.S.A.

[2]School of Molecular Sciences, Arizona State University, Tempe, Arizona 85287, U.S.A.

[3]GeoSoilEnviroCars, University of Chicago, Chicago, Illinois 60439, U.S.A.

Corresponding author: H. Piet, `helene.piet@asu.edu`

Abstract

Hydrogen (H) and sulfur (S) are light element candidates to enter the core of planetary bodies. Although Fe–S and Fe–H systems have been studied individually, the Fe–S–H ternary system has only been investigated up to 16 GPa and 1723 K. We have investigated the Fe–S–H system at pressures and temperatures (P–T) relevant to the cores of Mars-sized planets (up to 45 GPa and well above the melting temperature of FeS) in the laser-heated diamond anvil cell combined with *in situ* synchrotron X-ray diffraction. We found that at high P–T, Fe_3S is unstable if H exists in the system. Instead, separate Fe–H and Fe–S phases appear at 23–35 GPa. At pressures above 35 GPa, we found a new phase appearing while Fe–S phases disappear and Fe–H phases remain. Our analysis indicates that the new phase likely contains both S and H in the crystal structure (tentatively FeSH). The observed pressure dependent changes in the phase relation may be important for understanding the structure and dynamics of the Martian core and the cores of Mars-sized exoplanets.

Plain Language Summary

The metallic cores of planets and satellites are believed to contain significant amounts of light elements such as hydrogen and sulfur. To understand how a planetary core forms and evolves through time, it is important to know how iron alloys behave at the pressure-temperature conditions of the cores. The iron-hydrogen and the iron-sulfur alloy systems are well known, even at conditions of the Earth's core. However, the iron alloy systems with both sulfur and hydrogen together have only been studied for depths of smaller bodies like Ganymede. Using new experimental techniques, we study the behavior of the iron-hydrogen-sulfur alloy system at higher pressures and temperatures. We found that at intermediate depths, sulfur and hydrogen form two separate iron alloys, while at greater depths, a new iron alloy with both sulfur and hydrogen may form in Mars-sized planets' cores. This change in mineralogy with depth therefore suggests that the structure and dynamics in the cores of Mars-sized planets could be much more complex if hydrogen can be added to the region as a light element.

Key points

- Hydrogen makes Fe_3S unstable at the pressures and temperatures relevant to Mars-sized planetary cores.

- At 23–35 GPa, separate FeS and FeH phases are stable, whereas above 35 GPa, a new Fe alloy phase appears, which may contain both S and H.
- Crystallization from a Fe–S–H liquid would lead to a complex core structure.

1 Introduction

Significant amounts of light elements are necessary to explain the observed density deficit of the Earth's core from a pure Fe-Ni alloy [*Dziewonski and Anderson*, 1981]. Silicon, sulfur, oxygen, carbon, and hydrogen are strong candidates to lower the core's density because of their cosmochemical abundances and affinity with metallic iron at high pressures and temperatures [*Poirier*, 1994] during core formation [*Wade and Wood*, 2005]. Although a combination of light elements is more likely to explain the density deficit than just one element, a consensus on the combination itself has yet to be reached [*Badro et al.*, 2014].

Sulfur (S) and hydrogen (H) were both abundantly available in the proto-planetary disk from which planets and satellites in the solar system formed. Although S and H are both volatile elements at 1 bar, they show siderophile (iron-loving) behaviors at pressures relevant to core formation processes [*Badding et al.*, 1991; *Pépin et al.*, 2014; *Li and Agee*, 2001]. Fe–S and Fe–H systems, separately, have been extensively studied [e.g., *Badding et al.*, 1991; *Pépin et al.*, 2014; *Kamada et al.*, 2010; *Stewart et al.*, 2007; *Fei et al.*, 1995]. Experiments have shown that the solubility of H into metallic Fe increases significantly with increasing pressure [*Badding et al.*, 1991; *Pépin et al.*, 2014] up to FeH_5 [*Pépin et al.*, 2017]. The Fe–FeS system is eutectic up to 271 GPa, where Fe_3S is stable together with pure Fe [*Stewart et al.*, 2007; *Ozawa et al.*, 2013]. S and H have been shown to both significantly lower the melting temperature of pure Fe [*Fei et al.*, 1995; *Morard et al.*, 2007; *Kamada et al.*, 2010; *Sakamaki et al.*, 2009; *Hirose et al.*, 2019]. Low melting temperatures (like those of Fe_3S and FeH) could, for example, increase the longevity of a liquid core and therefore contribute to the dynamics of the region. S and H should therefore have important implications for planetary cores. A study up to 16 GPa reported the solubility of H into FeS, thus forming a $FeSH_x$ phase (where $x \simeq 0.3$) [*Shibazaki et al.*, 2011]. However, the behavior of the system is unknown beyond these conditions.

Because H is very volatile and highly reactive, it is a challenging element to study at high pressures and high temperatures. A few studies have investigated phase relations for hydrogen-involved ternary systems. *Narygina et al.* [2011] and *Ohta et al.* [2019] have

shown that when reacting pure Fe together with paraffin (C_nH_{2n+2}, $n > 5$) up to 68 GPa, FeC and FeH form separate solid phases under subsolidus conditions. *Hirose et al.* [2019] also showed that up to 127 GPa at liquidus conditions, H preferentially partitions into the liquid, thus limiting the solubility of C in the liquid. *Ohtani et al.* [2005] observed the formation of separate FeO and FeH phases when reacting Fe with H_2O below 84 GPa, whereas above 84 GPa, FeOOH and FeH were observed [*Liu et al.*, 2017; *Yuan et al.*, 2018]. On the other hand, H does not seem to alter the compressibility of hcp-FeSi or induce any phase separation like that observed for Fe–C and Fe–O systems [*Tagawa et al.*, 2016].

The co-solubility of H with another light element in iron alloy appears to be a complex variable of pressure, temperature and composition. It is therefore difficult to interpolate the geophysical implications of a ternary system from separate binary systems given the seemingly complex relationships between light elements. Whether it is by experimental design or not, studies using non pure H sources have to consider the potential effects of other elements, such as C in the case of paraffin, or oxidized conditions in the case of H_2O. While more ideal from a compositional point of view, the use of a pure H_2 source comes with its own set of experimental challenges: the high mobility and diffusivity of H at high P–T make diamond anvils much more brittle, therefore increasing the chance for experiment failure when a H medium is combined with conventional continuous wave laser heating in the diamond-anvil cell (DAC). Regardless, pure H_2 medium is the most ideal H source when studying the effect of H on any system, and recent experimental progress with the advent of pulse laser-heating systems [*Deemyad et al.*, 2005] combined with time-gated X-ray diffraction (XRD) [*Goncharov et al.*, 2010] now allow significant reduction of diamond embrittlement during experiments with pure H, while still providing XRD patterns of sufficient quality.

We have conducted experiments on the phase relations in the Fe–S–H system at pressures up to 45 GPa and temperatures above the melting of FeS, using laser-heated diamond-anvil cell combined with synchrotron X-ray diffraction for phase characterization at *in situ* high pressure and high temperature. We then discuss the potential implications of our experimental observations for the crystallization of cores of Mars-sized planetary bodies.

2 Experimental methods

2.1 Starting Materials

The pure Fe_3S sample was synthesized in a 1000 tons multi-anvil press at ASU following the method presented in *Kamada et al.* [2014a]. A Fe + FeS mixture was encapsulated in MgO capsule and brought to a pressure of 21 GPa using 8/3 cell assemblies. Heating was conducted in a few steps: 5 minutes at 1533 K for melting and homogenization of the mixture, then 30 minutes at 1413 K to favor the crystallization of Fe_3S grains and finally 1 hour at 1273 K to enhance the growth of Fe_3S grains. The sample was then quenched to room temperature and progressively brought back to room pressure overnight. Energy-dispersive spectroscopy chemical mapping in scattering electron microscopy (SEM) and XRD data were acquired after recovery to examine the chemical composition and crystal structure of synthesized crystals, respectively (see Fig. S1 and Tab. S1) and confirmed the purity and homogeneity of the sample.

We also explored other compositions along the Fe–FeS joint: Fe + Fe_3S mixture and FeS. Pure FeS was obtained from Alfa Aeasar chemicals. For the Fe + Fe_3S, we used a mechanical mixture of Fe and Fe_3S. Since only small amounts of multi-anvil samples were available, the mixture was not sufficiently homogeneous for maintaining the same compositions for diamond-anvil cell loadings. Therefore, we used the mixture data only to qualitatively supplement our main data from Fe_3S.

2.2 Diamond-anvil cell preparation

Pressures were achieved using diamond anvils ranging in size from 200 μm to 150 μm. We loaded a thin foil of the starting material into pre-indented and drilled rhenium gaskets. The rhenium gaskets were gold coated to reduce the diffusion of hydrogen into the gasket material, which can weaken the gasket and therefore result in anvil failure [*Pépin et al.*, 2014]. To ensure proper insulation from the diamonds during laser-heating, we propped the sample using small pieces of the same starting material. We used gold as a pressure marker [*Ye et al.*, 2017]. To prevent unwanted/unknown reactions between gold, hydrogen and the sample during high-temperature experiments, we chose not to mix gold with the sample but instead load it as a separate chip next to the sample. We then loaded pure hydrogen gas at a pressure of 1500 bar into the sample chamber using the hydrogen gas loading facility located at Arizona State University. After the gas loading, we compressed the cell to its target pres-

sure. In-house monitoring of pressure after hydrogen loading was enabled by the presence of a small ruby chip placed in the sample chamber prior to hydrogen loading [*Mao et al.*, 1986].

2.3 Synchrotron measurements

We performed synchrotron X-ray diffraction (XRD) at *in situ* high-pressure and high-temperature in the laser-heated diamond anvil cell. XRD patterns were acquired at the 13-IDD beamline of the GSECARS sector of the Advanced Photon Source. A 3×4 μm^2 monochromatic X-ray beam with energy of 30 keV or 37 keV was co-axially aligned with double-sided near-infrared laser-heating beam providing a 15×20 μm^2 heating spot. We used the pulsed-laser heating technique to prevent significant anvil embrittlement enhanced by hydrogen at high temperature [*Deemyad et al.*, 2005]. For this, the laser pulse was synchronized with gated X-ray and temperature detectors to allow acquisition of XRD patterns at in situ high $P-T$ [*Goncharov et al.*, 2010]. To obtain diffraction patterns in sufficiently high quality, we generated a series of 10^5 pulses to a repetition rate of 10 kHz and accumulated the obtained diffraction patterns during heating. After temperature quench at high pressure we measured XRD patterns in regular continuous-wave (CW) mode for higher quality.

The temperature was calculated by fitting a Planck equation to the thermal radiation spectra collected on both sides of the DAC assuming a grey-body approximation [*Prakapenka et al.*, 2008]. 2D diffraction images were collected using a Pilatus 1M CdTe detector. We used a LaB_6 standard to calibrate and correct distortions and detector distance (~200 mm) during integration from 2D images to 1D patterns in the Dioptas software [*Prescher and Prakapenka*, 2015]. We used the PeakPo software package for peak identification and unit-cell fitting [*Shim*, 2017].

2.4 Electron Probe Micro-Analysis

To resolve chemical compositions of the phases synthesized at high $P-T$, electron probe micro-analysis (EPMA) was performed on starting materials synthesized in the multi-anvil press, and on the recovered samples from the laser-heated diamond-anvil cell (LH-DAC). X-ray intensity mapping and semi-quantitative point analysis were performed at Arizona State University's Eyring Materials Center using a JEOL JXA-8530F. To avoid charge build-up, samples were coated with a thin conductive C-layer to increase electron conductivity and improve sample imaging and analysis. Sample imaging was mainly done using back

scattered electrons (BSE). For energy dispersive spectroscopy (EDS) X-ray intensity mapping, the electron microprobe was operated at 20 kV with a current of 75 nA and a dwell time of 50 ms, producing 128×96 pixel maps. For wavelength dispersive spectroscopy (WDS) X-ray intensity mapping, the microprobe was operated at 20 kV with a current of 100 nA and a dwelling time of 50 ms, resulting in 270×270 pixel maps.

Considering the beam penetration and the depth of electron interaction combined with small grain sizes of the phases from LHDAC experiments, EPMA could sample signal from underlying phases. This problem could have been reduced by making thin sections at the laser-heated spots using a focused ion beam (FIB). However, the recovered samples appear to be much weakened by intense chemical reaction with hydrogen, which should have been in liquid state during heating. Therefore, we chose EPMA which requires minimal processing of the mechanically weakened recovered samples.

3 Results and discussion

3.1 Fe_3S + H

We investigated the reaction between Fe_3S and pure hydrogen at pressures of 23–45 GPa and temperatures up to 4000 K. In all the runs, no reaction of Fe_3S with hydrogen was observed under cold compression to high pressures (i.e. before laser heating) (Fig. 1a), and the measured unit-cell volume of the phase is similar to that of pure Fe_3S reported at the same conditions [*Fei et al.*, 2000]. Therefore, we interpret that Fe_3S does not react with hydrogen at room temperature and high pressures. The behavior is in contrast with that of pure Fe metal where it has been consistently reported that Fe metal reacts with hydrogen at high pressures and 300 K and converts to double hexagonal close packed (dhcp) structure of FeH [*Badding et al.*, 1991].

After a Fe_3S sample was heated in a H medium to 2830 K at 28 GPa, the phase completely disappeared from the diffraction patterns (Fig. 1b). The instability of Fe_3S at 28 GPa is striking since Fe_3S is reported to be stable up to 271 GPa at 3300 K [*Ozawa et al.*, 2013] This observation shows that the behavior of Fe_3S is fundamentally different when H is present in the system. In place of Fe_3S at 28 GPa, we observed a mixture of dhcp-FeH and FeS(III). Although the measured unit-cell volume of dhcp-FeH is similar to what is expected at 28 GPa [*Pépin et al.*, 2014], FeS(III) has a noticeably greater unit-cell volume than reported at this pressure [*Kusaba et al.*, 1997] (Fig. S2), suggesting incorporation of H into the FeS(III)

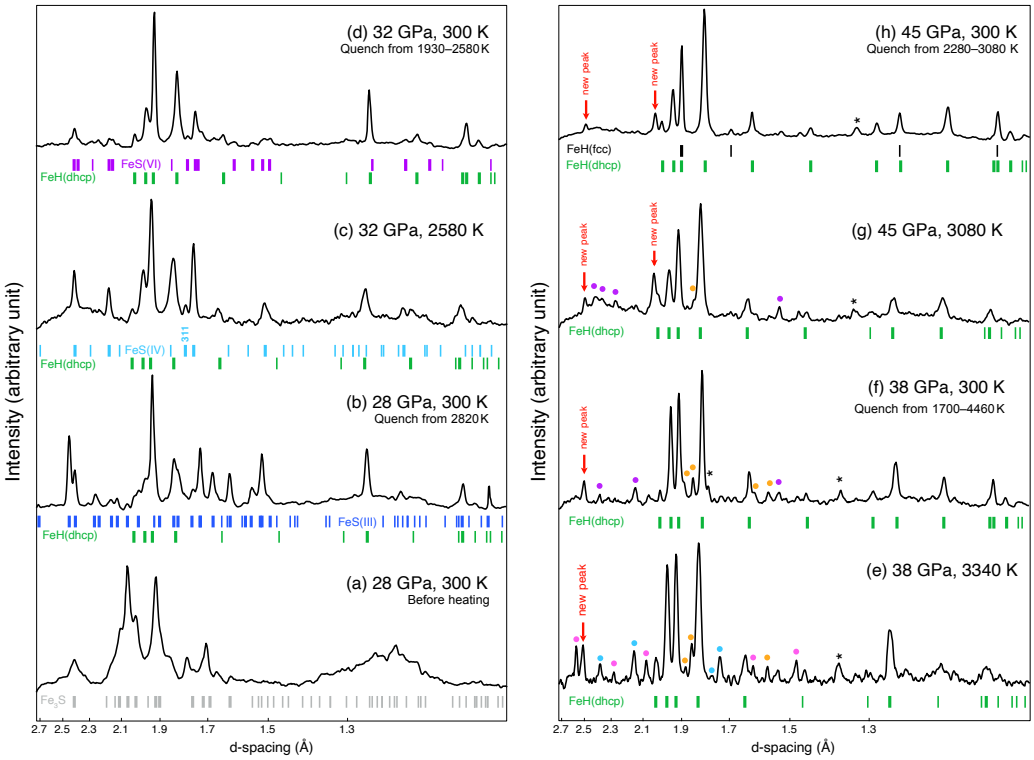

Figure 1. X-ray diffraction for runs starting with $Fe_3S + H_2$. The thin vertical ticks show all the expected *d*-spacing and intensity for a given phase and the thick vertical ticks highlight the observed ones. The colored dots highlight observed peaks from minor phases (orange: Fe_2S; purple: FeS(VI); cyan: FeS(IV); pink: FeS_2). Unidentified lines are indicated by $*$. (a) Only Fe_3S is present before heating; (b) Fe_3S is not stable and transforms into a mixture of dhcp-FeH, FeS(VI) and FeH_2 after temperature quench; (c) Similar instability of Fe_3S was observed at a higher pressure during in situ heating; (d) FeS(IV) transforms to FeS(VI) and dhcp-FeH is present after temperature quench; (e) Fe_3S is not stable and transforms into a mixture of dhcp-FeH, FeS(IV) and FeS_2 during heating at 38 GPa. New peaks (red arrows) appear at >38 GPa; (f) After temperature quench, new peaks present with dhcp-FeH, while FeS(IV) transforms to FeS(VI); (g) At 45 GPa and 3080 K, Fe_3S is not stable and transforms into a mixture of dhcp-FeH, FeS(VI) and a new phase; (h) After temperature quench, dhcp-FeH, FeS(VI) and the new peaks are still present.

structure. The heating temperature, 2820 K, at 28 GPa is above the melting temperature of FeS [*Boehler*, 1992], FeH [*Sakamaki et al.*, 2009], and the eutectic temperature of Fe–Fe_3S [*Kamada et al.*, 2010] (Fig. 2a). Therefore, we interprete that liquid Fe_3S crystallized into the observed FeS and FeH phases. At 32 GPa, the same trend continues: disappearance of Fe_3S and appearance of dhcp-FeH and FeS (Fig. 1c-d) upon heating. Again here, the heating temperatures are higher than the expected melting temperatures of FeS and FeH. FeS(IV) and its higher temperature polymorph FeS(V) both feature NiAs-type structures, resulting in very similar diffraction patterns. The observation of FeS(IV) instead of FeS(V) above 1900 K (by the diagnostic 311 peak; Fig. 1c) is discrepant from reports for H-free FeS in the literature [*Kavner et al.*, 2001; *Fei et al.*, 1995; *Urakawa et al.*, 2004; *Ohfuji et al.*, 2007]. The measured unit-cell volumes of FeS(IV) are somewhat higher than expected at 32 GPa [*Urakawa et al.*, 2004] (Fig. S2), which indicates that a small amount of H could stabilize FeS(IV) over FeS(V). Upon quench, FeS(IV) transforms to FeS(VI) (Fig. 1d), whereas in H-free systems, FeS(IV) was instead observed to transform to FeS(III) upon temperature quench [*Fei et al.*, 1995; *Urakawa et al.*, 2004; *Ohfuji et al.*, 2007]. *Ohfuji et al.* [2007] did observe that FeS(IV) transforms to FeS(VI) with heating above 1300 K, but here the transition is observed upon temperature quench and could be an effect of H. Therefore, while a majority of H is alloyed in Fe metal to form FeH when Fe_3S liquid crystallizes, some small amounts of H alloy with FeS phases and affect the phase behaviors.

At 38 GPa, unlike the results at lower pressures, we find a new peak appearing during heating at $d_{sp} = 2.87$ Å, which will be discussed later. A few weak lines also appear during or after heating. Although they can be assigned to either FeS_2 or *Pnma*-Fe_2S [*Zurkowski*, 2020], because these peaks are mainly from weak spots in diffraction images, their assignments are not conclusive. Given the low intensity of these phases, they are likely related to thermal gradients during laser heating. Therefore, we interpret that they are not stable phases at the $P - T$ conditions with hydrogen.

At 45 GPa and 3080 K, Fe_3S completely transforms into dhcp–FeH, and FeS(VI) (Fig. 1g). The previously observed new peak is again present here, as well as an additional strong new peak ($d_{sp} = 2.24$ Å). Weak peaks, which can be assigned to FeS_2 progressively disappear with further heating in the 2280–2590 K range, regardless of temperature, and could be caused by thermal heterogeneity during laser heating. Similarly, intensities of the peaks which can be assigned to FeS(VI) and Fe_2S decrease with further heating, and Fe_2S has completely disappeared with temperature quench. Dhcp-FeH and the new peaks, however, grow

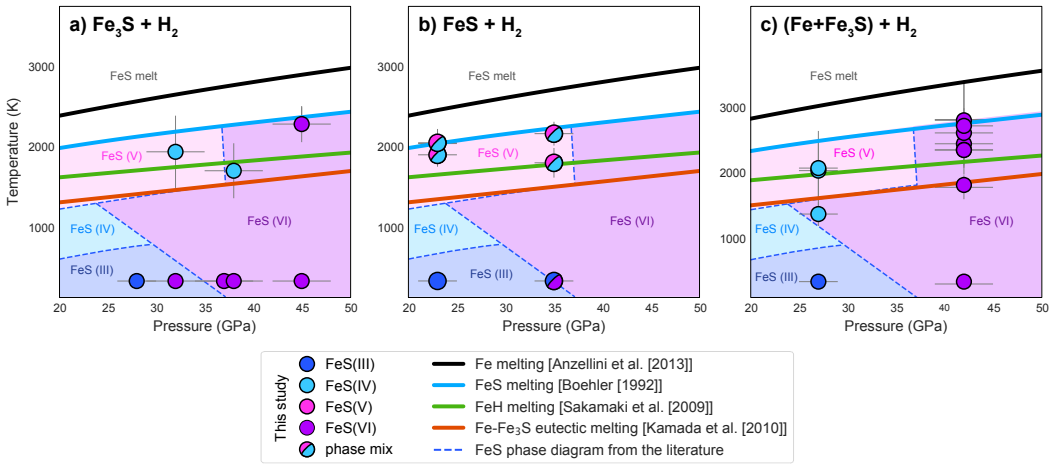

Figure 2. Pressure–temperature conditions for FeS phases in a hydrogen medium in: (a) $Fe_3S + H_2$, (b) $FeS + H_2$ and (c) $(Fe+Fe_3S) + H_2$ starting materials. In this figure, we show only the data points measured below FeS melting. The symbol colors refer to the observed polymorphs of FeS at the conditions (see legend). We also have some data points measured above melting temperatures of iron alloys and they can be found in Tab. S2. The reported polymorphs at 300 K are those observed after temperature quench. The solid lines represent the melting curves of different phases (black: pure Fe [*Anzellini et al.*, 2013], blue: FeS [*Boehler*, 1992], green: FeH [*Sakamaki et al.*, 2009], orange: eutectic for Fe–Fe_3S [*Kamada et al.*, 2010]). Stability fields for FeS polymorphs in H-free system are represented by different colors and boundaries are emphasized with blue dashed lines [*Fei et al.*, 1995; *Kavner et al.*, 2001; *Urakawa et al.*, 2004; *Ono and Kikegawa*, 2006; *Ohfuji et al.*, 2007].

stronger with subsequent heating and remain the major phases in the final quench (Fig. 1h). The stronger than expected intensity of the 004 dhcp-FeH peak (d_{sp} =2.05 Å at this pressure) in the pattern suggests that the observed peak intensity does not only result from the presence of dhcp-FeH. A legitimate candidate to explain the observation is fcc-FeH, which has been reported to form at high temperature at this pressure range [*Thompson et al.*, 2016; *Kato et al.*, 2020], and which 111 peak could account for the observed intensity.

3.2 FeS + H

To further understand the phase behavior of Fe–S–H system, we also studied pure FeS in a hydrogen medium using the same experimental procedure as for Fe_3S + H_2 at similar pressures. Before heating at 23 GPa, the pattern can be explained by a single FeS(III) phase. The measured unit-cell volume of the phase is slightly higher than that of pure FeS(III) at the same pressure (Fig. S2) [*Kusaba et al.*, 1997], suggesting some solubility of H in this FeS(III) phase even without heating. With heating, fcc-FeH appears in diffraction patterns as a major phase. Some minor peaks can also be assigned to dhcp-FeH (Fig. 3b). Dhcp-FeH was observed to be a more prominent phase in runs starting with Fe_3S. Although we do not have direct evidence for this, the prominence of fcc-FeH over dhcp-FeH in FeS + H_2 runs suggests that some S in the crystal structure may affect the stability of one structure with respect to another since the S content is the most notable difference between the Fe_3S + H_2 runs and the FeS + H_2 runs.

We also identify both FeS(IV) and FeS(V) at high temperature (Fig. 2b). FeS(V) was not observed in runs with the Fe_3S + H starting materials. Since FeS(V) is usually the stable polymorph at these $P - T$ conditions in H-free systems [*Ono and Kikegawa*, 2006], we attribute the existence of both FeS(IV) and FeS(V) to an incomplete reaction of FeS with H where FeS(IV) results from the reaction with H at high temperature and FeS(V) is the non reacted FeS phase. The absence of volume change from its expected volume at 23 GPa is also a good indicator that the phase did not react with hydrogen (Fig. S2). Upon temperature quench, both FeS phases transform to FeS(III) (Fig. 3b). The unit-cell volume for FeS(III) being higher than before heating [*Kusaba et al.*, 1997] suggests increased solubility of H in FeS(III) from laser heating.

At 35 GPa and 3674 K, FeS (III) in a pure hydrogen medium transforms to a FeS(IV)–FeS(V) mixture similarly to what is observed at 23 GPa. There are, however, a few impor-

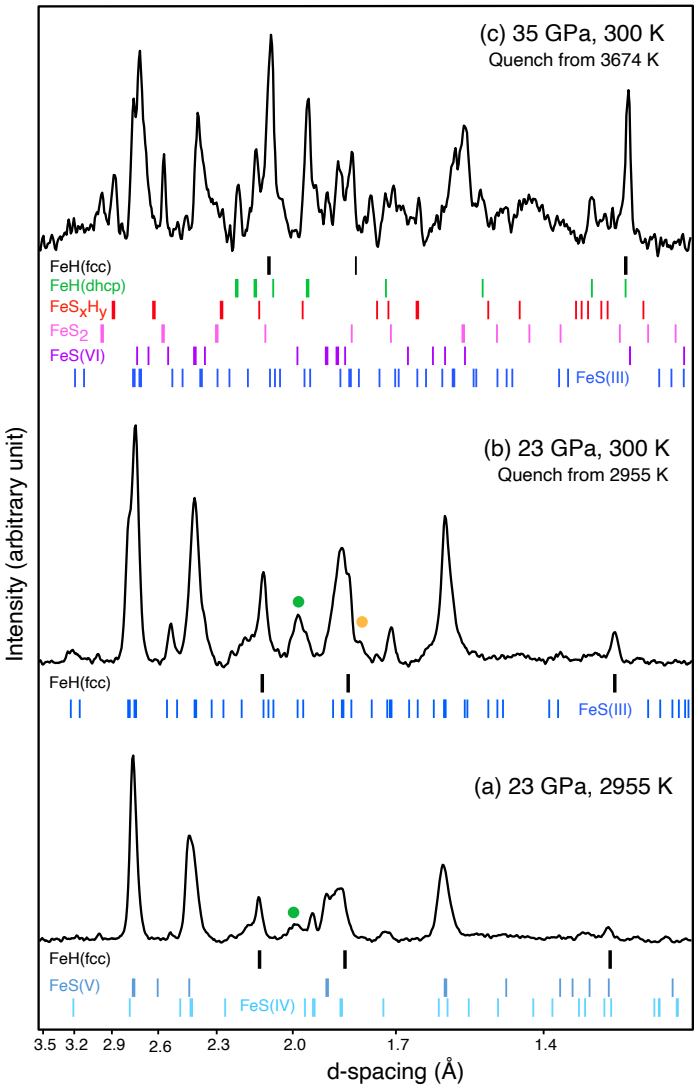

Figure 3. X-ray diffraction for runs starting with FeS + H_2. The thin vertical ticks show all the expected *d*-spacing and intensity for a given phase and the thick vertical ticks highlight the observed ones. The colored dots highlight observed peaks from minor phases (green: dhcp-FeH; orange: Fe_2S). (a) At 23 GPa and 2955 K, fcc-FeH and FeS(IV) form from the reaction of FeS and H_2, whereas FeS(V) most likely results from non reacted FeS with H_2. (b) Upon temperature quench FeS transforms entirely to FeS(III). Fcc-FeH remains a major phase and dhcp-FeH remains a minor phase. (c) Diffraction pattern measured after temperature quench from 3674 K at 35 GPa is more complex than at 23 GPa. The new phase (FeS_xH_y) is observed, as well as FeS (III and VI), FeS_2 and both fcc-FeH and dhcp-FeH are major phases here.

tant differences between the runs at 23 GPa and the one at 35 GPa. First, we found more enhanced diffraction intensities from dhcp-FeH (Fig. 3c). The different behavior might be related to extremely high temperature above melting achieved in this higher pressure run. Second, we observed the same new peaks found in Fe_3S + H runs. The number of phases observed in the diffraction pattern exceeds the number expected for thermal equilibrium in Fe–S–H ternary. Because heating was conducted to a temperature much above melting, it is possible that thermal gradients were more severe and therefore result in complex crystallization during temperature quench.

In most of the experiments for the FeS + H_2 starting materials, we observed FeH and FeS. The formation of FeH without S at lower pressures requires some amount of S either dissolved in the H medium or reacting with H to form a S-H phase. However, S-H phases would be challenging to detect in X-ray diffraction because of very low X-ray scattering cross sections expected for the phases. Therefore, within our resolution, the absence of S-H phase peaks cannot rule out the possibility of its existence in reaction product.

3.3 Fe + Fe_3S + H

Since no Fe–S alloy richer in Fe than Fe_3S exists, we used a mechanical mixture of Fe and Fe_3S as a proxy to study how increasing amounts of metallic Fe in the bulk system affects the results when reacted with H_2 (Tab. S2). At 27 GPa and 1100 K, we observed fcc-FeH and FeS(IV). FeS(IV) persisted to higher heating temperatures (up to 2670 K). Again, the presence of FeS(IV) instead of FeS(V) expected at these conditions (Fig. 2c), suggests that FeS(IV) might host a significant enough amount of H in order to stabilize the structure at the temperature. At 42 GPa and 2077 K, we observed peaks attributed to the new phase upon heating, which confirms what was observed for pure Fe_3S and FeS starting runs. We also observed FeH (mostly in dhcp). Although the existence of multiples of phases in this starting mixture makes the interpretation more complicated, the main features we observed in Fe_3S + H_2 runs and FeS + H_2 runs were reproduced in these experiments.

3.4 A new phase in Fe–S–H

Fig. 4 shows the pressure and temperature conditions for all the runs we conducted. In the figure, we highlighted the conditions where the new diffraction lines were observed.

The new peaks were observed only above 35 GPa regardless of the starting composition. The stability of the phase does not seem to have a strong temperature dependence either.

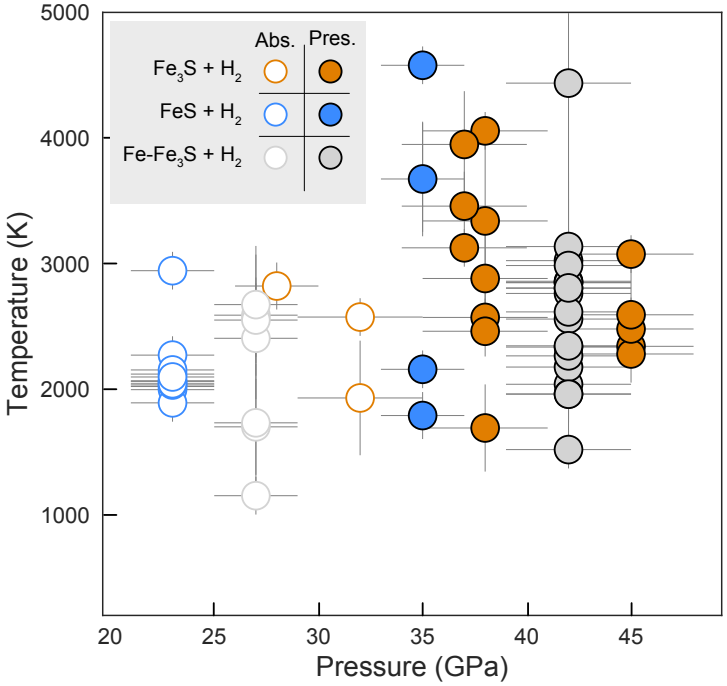

Figure 4. Pressure and temperature conditions for the observation of the new phase associated with the new diffraction peaks. The open and the close circles are for non-observation and observation of the new phase respectively.

Given the presence of Fe–S and Fe–H phases in our runs, a potential candidate to explain the observed new peaks is a counterpart hydrogen sulfide phase. Neither $I4/mcm$-H_3S nor $I222$-H_3S, however, provides a match for the observed new peaks in terms of expected peak position or intensity [*Strobel et al.*, 2011; *Duan et al.*, 2014]. Although we cannot completely exclude the formation of hydrogen sulfide in our runs, the relatively smaller X-ray scattering cross-section of H–S phases compared with iron-bearing phases, would make such a compound challenging to detect and therefore an unlikely source for the intense new lines observed in our diffraction patterns. Regarding the possibility for a Fe–S phase, *Shibazaki et al.* [2011] reported the formation of $FeSH_x$(IV) and $FeSH_x$(V) at 16.5 GPa and above 800 K. However, volume expanded versions of FeS(IV) and FeS(V) would only change the peak position.

The presence of FeH in our runs suggests that the new peaks could also be iron hydride. At the investigated $P-T$ range, the stable iron-hydrogen alloys are dhcp-FeH and fcc-FeH [*Badding et al.*, 1991; *Narygina et al.*, 2011]. We found that the observed new lines can be well indexed with a tetragonal unit cell. The positions of all four new peaks can be fit to a FeH_2-like tetragonal structure [*Pépin et al.*, 2014], albeit with an increased unit-cell volume by +60% uniformly along all three directions (Fig. 5 and Tab. S3). Increased hydrogen solubility in iron hydrides also leads to volume expansion and it was observed for interstitial hydrogen in fcc-FeH [*Narygina et al.*, 2011] and for molecular hydrogen in FeH_2 and FeH_5 [*Pépin et al.*, 2014, 2017] through the formation of additional layers of hydrogen. However, FeH_5, which was reported to form above 135 GPa [*Pépin et al.*, 2017], does not explain the new peaks (Fig. 5). Due to the layered nature of the FeH_2 structure (alternating layers of Fe and H), it is unlikely that more H would explain the observed homogeneous volume expansion to all three directions, but rather would be directional. It is worth noting that FeH_2 was reported to appear only above 67 GPa [*Pépin et al.*, 2014]. Therefore, formation of a similar structure at significantly lower pressures requires some other stabilizing sources. Since S can also increase the unit-cell volume, this phase may contain both S and H.

We constructed a diffraction intensity map for the new phase using the most intense line. The map shows that the phase is populated mostly near the rim of the laser heated spot. (Fig. 5b). The chemical maps of the same heated spot also reveals a rim like structure around the hot spot (Fig. 5b). The areas can be divided into: i) non reacted material around the heated area of Fe_3S composition as confirmed by point analysis (the green area in the S map), ii) S-poor/free areas at the laser heated center most likely the remnants of unquenchable FeH converted into Fe metal and iii) S-rich areas at the rim of the heated spot (the red rim in the S map). As shown in the figure, the new phase is located in the S-rich area and therefore should contain higher S content than the starting material, Fe_3S. The S-rich rim area should also have FeS(VI) as well as the new phase according to our X-ray diffraction analysis. Unfortunately, our EPMA results cannot resolve the difference in Fe:S ratio between FeS(VI) and the new phase. The reason for this is that the typical grain size of the phases in LHDAC experiments is a few hundreds of nanometers. The thickness of the recovered sample is approximately 10 μm and the excitation depths by the electron beam should be large enough for the thickness. Therefore, phases beneath the surface could contaminate the chemical composition measured in the EMPA of the LHDAC recovered sample. For accurate measurements, thinning of the heated area using focused ion beam (FIB) and chemical anal-

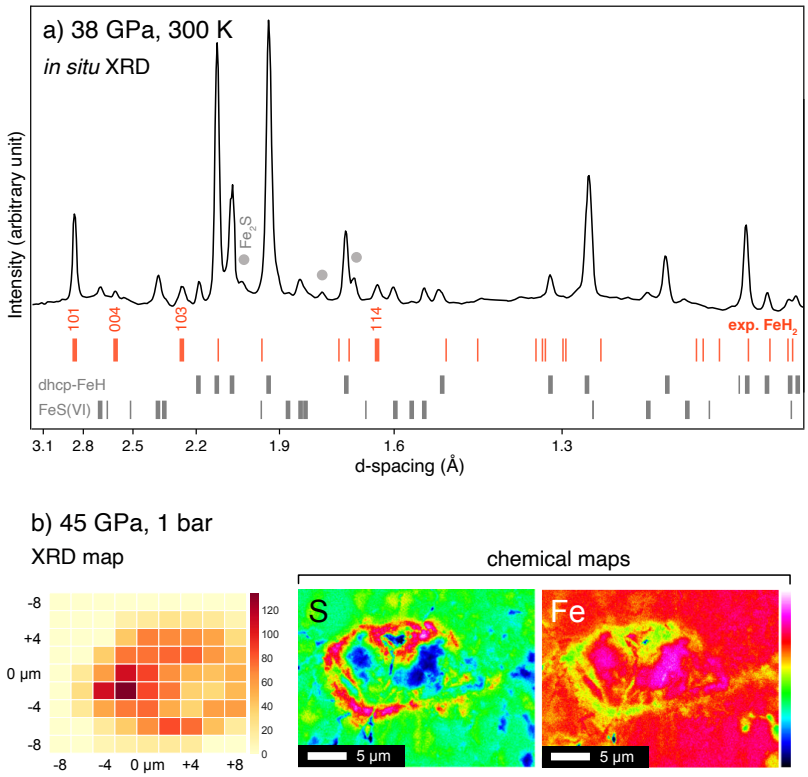

Figure 5. a) An X-ray diffraction pattern for the new phase at 38 GPa and 300 K upon temperature quench after reaction of $Fe_3S + H_2$ at temperatures in the 1700–4460 K range. The thin vertical ticks show all the expected *d*-spacing and intensity for a given phase and the thick vertical ticks highlight the observed ones. The expanded FeH_2 (red ticks) structure provides the best fit for the new observed peaks with four peaks uniquely matching without overlaps with other phases (bold ticks). Additionally, peaks at 2.1, 1.7, and 1.1 Å, while overlapping peaks from other phases, can also match and to some degree enhance the intensity of observed peaks. The gray dots indicate weak peaks which can be assigned to a small amount of Fe_2S. b) A map of the diffraction intensity of the FeS_xH_y 101 peak in the laser heated area from run r320 at 45 GPa (starting with $Fe_3S + H_2$) (left). The map was constructed from diffraction patterns collected after temperature quench in a 16×16 μm grid with 2 μm steps. The map shows that the phase is populated in the outer part of the heated area. Composition maps for S and Fe (right) of the recovered heated area show that the center of the heated spot is mostly Fe-rich while the edge is more S-rich.

ysis in Transmission Electron Microscopy would be required. However, samples synthesized in a H medium are mechanically weak and were not suitable such sample processing.

While the exact ratio between Fe and S is unknown for the new phase, as discussed, EPMA results combined with XRD analysis can constrain the ratio to be close to 1:1. We performed unit-cell volume measurement during decompression to 1 bar for the new phase synthesized in two runs (r220 and r231c; Fig. 6). While the measured volume of the new phase is very close to that of FeS(VI), it is systematically greater throughout the pressure range. Increasing solubility of H in iron hydrides at high pressure has shown to contribute to increase in unit-cell volumes [*Badding et al.*, 1991; *Narygina et al.*, 2011; *Pépin et al.*, 2014]. Fitting to a Vinet equation [*Vinet et al.*, 1987] for fixed pressure derivative of bulk modulus ($K' = 4$) yielded $V_0 = 110.4(5)$ and $K_0 = 159(7)$ for the new phase. The equation of state curve of the new phase is nearly parallel to that of FeS(VI) and therefore the volume difference between FeS(VI) and the new phase remains nearly constant within the pressure range.

Fig. 6 shows the volume per one Fe of the phases in the Fe–H and Fe–S system. Such a representation gives qualitative insights on how substituting S and H would increase the volume of Fe alloys. However, this representation requires knowledge of the number of formula units in the unit-cell (Z). The Z number is unknown for the new FeS_xH_y phase. Since we indexed the diffraction lines of the new phase to a tetragonal FeH_2-like structure, we choose to use the same Z number (4). We calculated the volume differences between hcp-Fe and different iron sulfides and iron hydrides, as well as between iron hydrides and iron sulfides themselves (Tab. S4). We obtained an average value for $\Delta V_{\mathrm{H}} = 2.02$ Å^3 corresponding to the average volume increase caused by one atom of H. Therefore, the near constant volume difference between FeS(VI) and the new phase can be explained by $y \simeq 1$ for FeS_xH_y where $x = 1$ from the EMPA data. While the assignment for the new phase here remains tentative because of the uncertainties in the crystal structure, from the arguments above built from our observations, it is reasonable to assume that the new phase is close to FeSH ($x = 1$ and $y = 1$ for FeS_xH_y). Therefore, in the remainder of the text we refer to the new phase as FeSH.

In pure Fe, H escapes from the crystal structure during decompression [*Okuchi*, 1997]. As H expands the unit-cell volume, H loss can result in a sudden volume decrease. For the new FeSH phase, we did not observe any significant volume decrease during decompression and the measured P–V data show a smooth trend extended to near 1 bar (Fig. 6). At 1 bar,

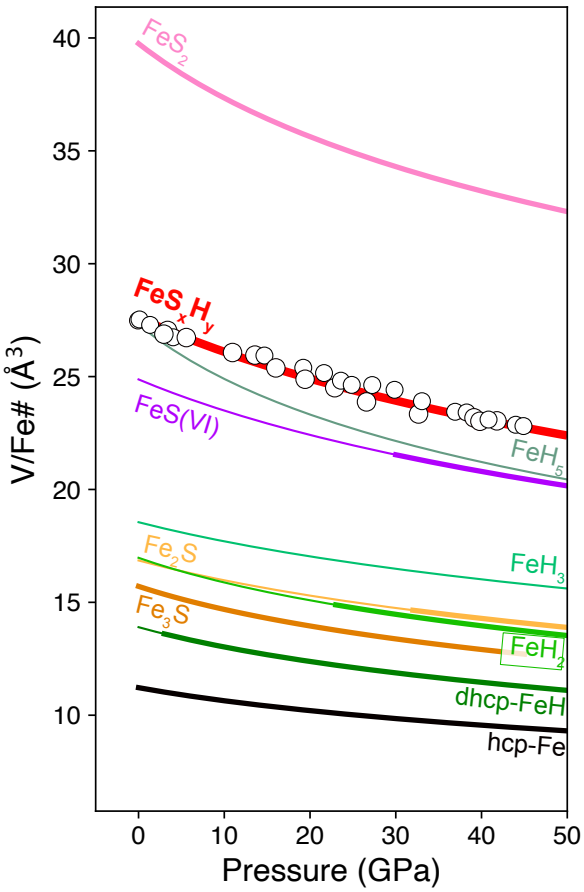

Figure 6. Pressure-volume relation of the new phase (FeS_xH_y, open circles) and the fitted equation of state (the thick red curve). We also show other phases in the Fe–S–H system from the literature for comparison (thick lines correspond to the pressure range at which the phase is observed to be stable; thin lines correspond to pressure range outside the phase stability where the fitted volume is extrapolated). Fe: *Dewaele et al.* [2006]; dhcp-FeH, FeH_2 and FeH_3: *Pépin et al.* [2014]; FeH_5: *Pépin et al.* [2017]; Fe_3S: *Kamada et al.* [2014b]; Fe_2S: *Zurkowski* [2020]; FeS(VI): *Ono and Kikegawa* [2006]; FeS_2: *Merkel et al.* [2002]. The unit-cell volumes are divided by the number of Fe atoms in the unit-cell. Note that we assume the new phase has the same number of Fe atom as regular FeH_2, which is 4.

the diffraction patterns of the sample quenched from 42 GPa show some new diffraction peaks as well as those existing at high pressures and assigned to the new phase (Fig. S3). The new lines appearing in the quench diffraction pattern could not be indexed with any known phases in Fe–S. It is feasible that FeSH may convert to a different crystal structure (either partially or completely) at 1 bar. Therefore, it is difficult to index the diffraction lines and the volume of the new phase remains uncertain at 1 bar.

4 Discussion

4.1 Phase relations in Fe–S–H up to 45 GPa

In all our experimental runs, we observed the striking disappearance of Fe_3S upon heating in a H-rich environment, regardless of pressure, temperature, and starting composition between Fe and FeS. The formation of FeH (dhcp and or fcc) is also common to all the runs. The differences observed between runs are whether FeS or FeSH was the main S-bearing phase at high pressure and high temperature. Although we do not have tight constraints on the melting behaviors of the studied system, we observed some clear pressure-dependent changes in the Fe_3S + H_2 experiments. Based on the information, we built provisional ternary Fe–S–H phase diagrams in Fig. 7.

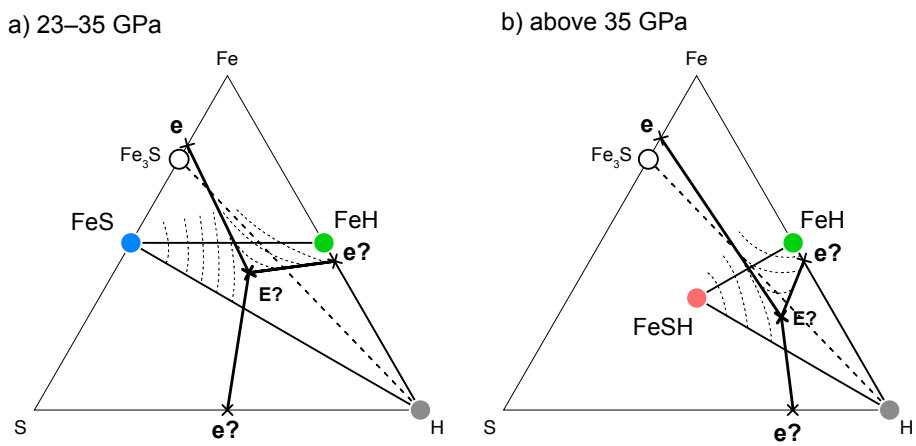

Figure 7. Provisional ternary Fe–S–H phase diagrams at 23–35 GPa (a) and above 35 GPa (b). *e*'s show the eutectic points in the Fe–S, Fe–H, and H-S binaries and *E* is the eutectic of the ternary. The colored circles show major phases observed at the pressures. The thick dashed lines connect the starting phases. The thin dashed lines represent possible isotherms. Note that the details of these diagrams remain uncertain and therefore the diagrams should be regarded as tentative.

At 23–35 GPa, we observed FeH and FeS phases in temperature quench (Fig. 7a). However, according to Gibbs' phase rule, if thermodynamical equilibrium is reached (possibly locally in LHDAC), three phases are expected for a degree of freedom of 2. Although the third phase remains uncertain, it should not contain Fe, otherwise it would appear in XRD patterns. Therefore, we tentatively assign the third phase to H. It is feasible that a H-S phase instead is stable in our experimental runs. The Fe–S binary phase diagram is well constrained at pressures in the 23–40 GPa range [*Stewart et al.*, 2007] and features a eutectic behavior with eutectic composition close to Fe_3S at pressures below 35 GPa. The Fe–H binary phase diagram, on the other hand, is less well constrained but likely features a solid-solution for FeH_x where $x \leq 1$. *Shibazaki et al.* [2014] proposed a Fe–H binary phase diagram featuring a eutectic for $x > 1$ in FeH_x at 15 GPa. However, the subsequent discovery of FeH_2, FeH_3 [*Pépin et al.*, 2014] and FeH_5 [*Pépin et al.*, 2017] at higher pressures raises questions on the position of the eutectic along the Fe–H joint. Although many aspects of the phase diagram shown in Fig. 7a remains tentative, the crystallization of the FeS and FeH phases in our study at the pressure range is at least consistent with a global ternary eutectic point in the phase diagram.

Above 35 GPa after extended cycles of heating runs, only FeH and FeSH remained from the reaction of Fe_3S with H_2, whereas FeS almost completely disappears (Fig. 7b). Similarly to the case at 23–35 GPa, we assume that either H or H-S phase exists as the third phase. The key observation at this pressure range is that FeS is unlikely stable anymore and a phase including both S and H may appear in the phase diagram. Assuming that eutectic behavior along all three joints persists with increasing pressure, the position of the ternary eutectic may move towards the H end-member. However, the precise positions of the eutectic points remain to be constrained through additional experiments.

4.2 Implications for crystallization of Mars-sized planetary cores

The pressure range we studied for Fe–S–H overlaps with the range expected for the Martian core, 20–40 GPa [*Helffrich*, 2017]. For the Martian core, sulfur has been considered as the main light element based on its abundance in Martian meteorites and theoretical models of nebular condensation [*Dreibus and Wänke*, 1985; *Wänke and Dreibus*, 1988; *Lodders and Fegley*, 1997]. Although there are different views [*Wang and Becker*, 2017], existing models prefer 14–17% of S in the Martian core [*Gaetani and Grove*, 1997; *Urakawa et al.*, 2004; *Khan et al.*, 2017], which is close to Fe_3S. The amount of hydrogen stored in the Mar-

tian core is currently unknown. For the Martian mantle, recent estimates (100–300 wt ppm in H_2O) are at least similar to that of the Earth's mantle [*Leshin*, 2000; *McCubbin et al.*, 2010; *Hallis et al.*, 2012; *Usui et al.*, 2012]. Therefore, H remains as a viable candidate for a light element in the Martian core, as it can partition preferentially to the core from its affinity to metal at high pressures [*Okuchi*, 1997]. Although further improvements are expected, recent InSight data analysis found a much larger size for the Martian core, which may require a lower density than previously believed [*Stähler et al.*, 2021]. While more S can lower the density, the low density could also be explained by the presence of other light elements together with S. Because it can severely lower the melting temperature of iron metal [*Sakamaki et al.*, 2009], hydrogen could explain largely molten state of the present-day core proposed by a geophysical study [*Yoder et al.*, 2003]. Our experimental study also provides essential data to model the cores of Mars-sized planets found outside of the solar system [*Jontof-Hutter et al.*, 2015]. While detection and mass measurement are very challenging because of their small size, with their potential habitability and improved technology in coming missions, more data will likely be available for Mars-sized exoplanets.

According to our experimental observations, at 23–35 GPa (therefore, at much of the Martian core or at the core of sub-Mars), either FeS or FeH would crystallize first depending on the S/H ratio of the system. For example, if the bulk composition of the system is on the S-rich side (left of the eutectic line in Fig. 7a), FeS would likely be the first solid to crystallize and the liquid would become progressively enriched in H as crystallization of FeS proceeds. Layering of the core would then depend on the density contrast between the different phases, as well as mixing properties and local dynamics at play. The density difference between liquid FeH and liquid FeS is not known. However, solid FeH is denser than solid FeS because H tends to be incorporated in the interstitial site of the densely packed structure of Fe. If such relationship is applicable between solid FeS and liquid FeH, solid FeS could even "float" at the outer part of the core. Above 35 GPa (therefore, at the innermost Martian core or at the cores of super-Mars and sub-Earths), the appearance of a new FeSH phase could change the crystallization of the core. In this case, either FeSH or FeH would crystallize first. H would likely decrease the melting temperature of the new phase below that of FeS, but whether it would decrease the melting temperature below that of FeH is unknown. A few important measurements are therefore to be made to further understand Fe–S–H ternary in Mars-sized rocky planets' cores. Measurements of melting of FeSH are needed to further constrain the crystallization behavior of the system above 35 GPa. Our data mostly reside on

the H rich side of the Fe–S–H ternary (Fig. 7). Although some of the phases we identified here could still appear in low H systems, it would be important to conduct measurements on systems with smaller amounts of H, which would be more relevant for planets with a smaller amount of H.

Although not directly relevant to the Earth, our results shed additional light on the complexity of light element partitioning between solid and liquid Fe, especially when H is involved. The observed density difference between the solid and liquid Earth's core suggests that the liquid outer core is enriched in light elements with respect to the solid inner core [*Birch*, 1952; *Poirier*, 1994]. Melting experiments on Fe–S alloys have shown that all light elements do not necessarily preferentially partition into liquid Fe. *Mori et al.* [2017] showed that the partition coefficient of S between solid and liquid iron increases with increasing pressure and the trend persists up to 254 GPa, which in turn suggests that with increasing pressure S tends to be more soluble into solid Fe than into liquid Fe. The preferential partitioning of S towards solid Fe with increasing pressure was later confirmed by *Yokoo et al.* [2019] who performed melting experiments on the Fe–O–S system up to 208 GPa. Our study of the Fe–S–H system at 23–35 GPa confirms what has been observed in the literature for Fe–C–H [*Narygina et al.*, 2011; *Ohta et al.*, 2019; *Hirose et al.*, 2019] and Fe–O–H up to 80 GPa [*Ohtani et al.*, 2005; *Liu et al.*, 2017; *Yuan et al.*, 2018] : H may not necessary alloy with other light elements but could preferentially partition into a phase that does not contain the other light element. However, like in the Fe–O–H system above 80 GPa with the formation of FeOOH, pressure appears to promote the formation of a ternary alloy (FeSH, the new phase we observed) in Fe–S–H as well, albeit at lower pressure. The relevance of FeSH for Earth-size planets remains to be tested at the required pressures, temperature and compositional conditions. If this behavior was to persist up to Earth's core pressure, and given that S prefers solid Fe, upon crystallization of a Fe–S–H rich core, an inner core could be enriched in S, whereas the liquid outer core could be enriched in H. First principle studies have shown that H can explain the density and compressional velocity of the Earth's outer core and therefore could be the primary light element in the outer core up to 1 wt.% [*Umemoto and Hirose*, 2015]. However, *Caracas* [2015] showed that solid Fe–H cannot explain the shear velocities observed in the inner outer core. Therefore, another light element like S, or a combination of light elements with an affinity for solid iron could be the primary light element(s) in the inner core.

Acknowledgement

The work has been supported by NSF-AST2005567 and NASA-80NSSC18K0353 grants. H.P., and S.-H.S. were supported partially by the Keck Foundation. The results reported herein benefit from collaborations and information exchange within NASA's Nexus for Exoplanet System Science (NExSS) research coordination network sponsored by NASA's Science Mission Directorate. Synchrotron experiments were conducted at GeoSoilEnviroCARS (University of Chicago, Sector 13), Advanced Photon Source (APS). GeoSoilEnviroCARS is supported by the NSF-Earth Science (EAR-1634415) and DOE-GeoScience (DE-FG02-94ER14466). APS is supported by DOE-BES under contract DE-AC02-06CH11357. We acknowledge the use of facilities within the Eyring Materials Center at Arizona State University supported in part by NNCI-ECCS-1542160. We would also like to acknowledge Axel Wittmann from the Eyring Materials Center at Arizona State University supported in part by NNCI-ECCS-1542160 for his assistance with EPMA measurements.

Data Availability Statement

Datasets for this research are included in this paper (and its supplementary information files): *Piet et al.* [2021].

References

Anzellini, S., A. Dewaele, M. Mezouar, P. Loubeyre, and G. Morard (2013), Melting of iron at Earth's inner core boundary based on fast X-ray diffraction, *Science*, *340*(6131), 464–466.

Badding, J. V., R. Hemley, and H. Mao (1991), High-pressure chemistry of hydrogen in metals: In situ study of iron hydride, *Science*, *253*(5018), 421–424.

Badro, J., A. S. Côté, and J. P. Brodholt (2014), A seismologically consistent compositional model of Earth's core, *Proceedings of the National Academy of Sciences*, *111*(21), 7542–7545.

Birch, F. (1952), Elasticity and constitution of the Earth's interior, *Journal of Geophysical Research*, *57*(2), 227–286.

Boehler, R. (1992), Melting of the FeFeO and the FeFeS systems at high pressure: constraints on core temperatures, *Earth and Planetary Science Letters*, *111*(2-4), 217–227.

Caracas, R. (2015), The influence of hydrogen on the seismic properties of solid iron, *Geophysical Research Letters*, *42*(10), 3780–3785.

Deemyad, S., E. Sterer, C. Barthel, S. Rekhi, J. Tempere, and I. F. Silvera (2005), Pulsed laser heating and temperature determination in a diamond anvil cell, *Review of scientific instruments*, *76*(12), 125,104.

Dewaele, A., P. Loubeyre, F. Occelli, M. Mezouar, P. I. Dorogokupets, and M. Torrent (2006), Quasihydrostatic equation of state of iron above 2 Mbar, *Physical Review Letters*, *97*(21), 215,504.

Dreibus, G., and H. Wänke (1985), Mars, a volatile-rich planet, *Meteoritics*, *20*, 367–381.

Duan, D., Y. Liu, F. Tian, D. Li, X. Huang, Z. Zhao, H. Yu, B. Liu, W. Tian, and T. Cui (2014), Pressure-induced metallization of dense (H2S)2H2 with high-Tc superconductivity, *Scientific reports*, *4*, 6968.

Dziewonski, A. M., and D. L. Anderson (1981), Preliminary reference Earth model, *Physics of the earth and planetary interiors*, *25*(4), 297–356.

Fei, Y., C. T. Prewitt, H.-k. Mao, and C. M. Bertka (1995), Structure and density of FeS at high pressure and high temperature and the internal structure of Mars, *Science*, *268*(5219), 1892–1894.

Fei, Y., J. Li, C. M. Bertka, and C. T. Prewitt (2000), Structure type and bulk modulus of Fe3S, a new iron-sulfur compound, *American Mineralogist*, *85*(11-12), 1830–1833.

Gaetani, G. A., and T. L. Grove (1997), Partitioning of moderately siderophile elements among olivine, silicate melt, and sulfide melt: Constraints on core formation in the Earth and Mars, *61*, 1829–1846.

Goncharov, A. F., V. B. Prakapenka, V. V. Struzhkin, I. Kantor, M. L. Rivers, and D. A. Dalton (2010), X-ray diffraction in the pulsed laser heated diamond anvil cell, *Review of Scientific Instruments*, *81*(11), 113,902.

Hallis, L. J., G. J. Taylor, K. Nagashima, and G. R. Huss (2012), Magmatic water in the martian meteorite nakhla, *359*, 84–92.

Helffrich, G. (2017), Mars core structure—concise review and anticipated insights from InSight, *Progress in Earth and Planetary Science*, *4*(1), 1–14.

Hirose, K., S. Tagawa, Y. Kuwayama, R. Sinmyo, G. Morard, Y. Ohishi, and H. Genda (2019), Hydrogen limits carbon in liquid iron, *Geophysical Research Letters*, *46*(10), 5190–5197.

Jontof-Hutter, D., J. F. Rowe, J. J. Lissauer, D. C. Fabrycky, and E. B. Ford (2015), The mass of the Mars-sized exoplanet Kepler-138b from transit timing, *Nature*, *522*(7556), 321–323.

Kamada, S., H. Terasaki, E. Ohtani, T. Sakai, T. Kikegawa, Y. Ohishi, N. Hirao, N. Sata, and T. Kondo (2010), Phase relationships of the Fe–FeS system in conditions up to the Earth's outer core, *Earth and Planetary Science Letters*, *294*(1-2), 94–100.

Kamada, S., E. Ohtani, H. Fukui, T. Sakai, H. Terasaki, S. Takahashi, Y. Shibazaki, S. Tsutsui, A. Q. Baron, N. Hirao, et al. (2014a), The sound velocity measurements of Fe3S, *American Mineralogist*, *99*(1), 98–251.

Kamada, S., E. Ohtani, H. Terasaki, T. Sakai, S. Takahashi, N. Hirao, and Y. Ohishi (2014b), Equation of state of Fe3S at room temperature up to 2 megabars, *Physics of the Earth and Planetary Interiors*, *228*, 106–113.

Kato, C., K. Umemoto, K. Ohta, S. Tagawa, K. Hirose, and Y. Ohishi (2020), Stability of fcc phase FeH to 137 GPa, *American Mineralogist: Journal of Earth and Planetary Materials*, *105*(6), 917–921.

Kavner, A., T. S. Duffy, and G. Shen (2001), Phase stability and density of FeS at high pressures and temperatures: implications for the interior structure of Mars, *Earth and Planetary Science Letters*, *185*(1-2), 25–33.

Khan, A., C. Liebske, A. Rozel, A. Rivoldini, F. Nimmo, J. A. D. Connoly, A.-C. Plesa, and D. Giardini (2017), A geophysical perspective on the bulk composition of Mars, *J. Geophys. Res.*, doi:10.1002/2017JE005371.

Kusaba, K., Y. Syono, T. Kikegawa, and O. Shimomura (1997), Structure of FeS under high pressure, *Journal of Physics and Chemistry of Solids*, *58*(2), 241–246.

Leshin, L. A. (2000), Insights into martian water reservoirs from analyses of martian meteorite QUE94201, *Geophys. Res. Lett.*, *27*, 2017–2020.

Li, J., and C. Agee (2001), Element partitioning constraints on the light element composition of the Earth's core, *Geophysical Research Letters*, *28*(1), 81–84.

Liu, J., Q. Hu, D. Y. Kim, Z. Wu, W. Wang, Y. Xiao, P. Chow, Y. Meng, V. B. Prakapenka, H.-K. Mao, et al. (2017), Hydrogen-bearing iron peroxide and the origin of ultralow-velocity zones, *Nature*, *551*(7681), 494–497.

Lodders, K., and B. Fegley (1997), An oxygen isotope model for the composition of Mars, *126*, 373–394.

Mao, H., J.-A. Xu, and P. Bell (1986), Calibration of the ruby pressure gauge to 800 kbar under quasi-hydrostatic conditions, *Journal of Geophysical Research: Solid Earth*, *91*(B5), 4673–4676.

McCubbin, F. M., A. Smirnov, H. Nekvasil, J. Wang, E. Hauri, and D. H. Lindsley (2010), Hydrous magmatism on Mars: A source of water for the surface and subsurface during the amazonian, *292*, 132–138.

Merkel, S., A. Jephcoat, J. Shu, H.-K. Mao, P. Gillet, and R. Hemley (2002), Equation of state, elasticity, and shear strength of pyrite under high pressure, *Physics and chemistry of minerals*, *29*(1), 1–9.

Morard, G., C. Sanloup, G. Fiquet, M. Mezouar, N. Rey, R. Poloni, and P. Beck (2007), Structure of eutectic Fe–FeS melts to pressures up to 17 GPa: implications for planetary cores, *Earth and Planetary Science Letters*, *263*(1-2), 128–139.

Mori, Y., H. Ozawa, K. Hirose, R. Sinmyo, S. Tateno, G. Morard, and Y. Ohishi (2017), Melting experiments on Fe–Fe3S system to 254 GPa, *Earth and Planetary Science Letters*, *464*, 135–141.

Narygina, O., L. S. Dubrovinsky, C. A. McCammon, A. Kurnosov, I. Y. Kantor, V. B. Prakapenka, and N. A. Dubrovinskaia (2011), X-ray diffraction and Mössbauer spectroscopy study of fcc iron hydride FeH at high pressures and implications for the composition of the Earth's core, *Earth and Planetary Science Letters*, *307*(3-4), 409–414.

Ohfuji, H., N. Sata, H. Kobayashi, Y. Ohishi, K. Hirose, and T. Irifune (2007), A new high-pressure and high-temperature polymorph of FeS, *Physics and Chemistry of Minerals*, *34*(5), 335–343.

Ohta, K., S. Suehiro, K. Hirose, and Y. Ohishi (2019), Electrical resistivity of fcc phase iron hydrides at high pressures and temperatures, *Comptes Rendus Geoscience*, *351*(2-3), 147–153.

Ohtani, E., N. Hirao, T. Kondo, M. Ito, and T. Kikegawa (2005), Iron-water reaction at high pressure and temperature, and hydrogen transport into the core, *Physics and chemistry of minerals*, *32*(1), 77–82.

Okuchi, T. (1997), Hydrogen partitioning into molten iron at high pressure: implications for Earth's core, *Science*, *278*(5344), 1781–1784.

Ono, S., and T. Kikegawa (2006), High-pressure study of FeS, between 20 and 120 GPa, using synchrotron X-ray powder diffraction, *American Mineralogist*, *91*(11-12), 1941–1944.

Ozawa, H., K. Hirose, T. Suzuki, Y. Ohishi, and N. Hirao (2013), Decomposition of Fe3S above 250 GPa, *Geophysical research letters*, *40*(18), 4845–4849.

Pépin, C., G. Geneste, A. Dewaele, M. Mezouar, and P. Loubeyre (2017), Synthesis of FeH5: A layered structure with atomic hydrogen slabs, *Science*, *357*(6349), 382–385.

Pépin, C. M., A. Dewaele, G. Geneste, P. Loubeyre, and M. Mezouar (2014), New iron hydrides under high pressure, *Physical review letters*, *113*(26), 265,504.

Piet, H., K. Leinenweber, E. Greenberg, V. B. Prakapenka, and S.-H. Shim (2021), Effects of hydrogen on the phase relations in Fe–FeS at pressures of Mars-sized bodies – Datasets, doi:10.5281/zenodo.4738360.

Poirier, J.-P. (1994), Light elements in the earth's outer core: a critical review, *Physics of the earth and planetary interiors*, *85*(3-4), 319–337.

Prakapenka, V., A. Kubo, A. Kuznetsov, A. Laskin, O. Shkurikhin, P. Dera, M. Rivers, and S. Sutton (2008), Advanced flat top laser heating system for high pressure research at GSECARS: application to the melting behavior of germanium, *High Pressure Research*, *28*(3), 225–235.

Prescher, C., and V. B. Prakapenka (2015), DIOPTAS: a program for reduction of two-dimensional X-ray diffraction data and data exploration, *High Pressure Research*, *35*(3), 223–230.

Sakamaki, K., E. Takahashi, Y. Nakajima, Y. Nishihara, K. Funakoshi, T. Suzuki, and Y. Fukai (2009), Melting phase relation of FeHx up to 20 GPa: Implication for the temperature of the Earth's core, *Physics of the Earth and Planetary Interiors*, *174*(1-4), 192–201.

Shibazaki, Y., E. Ohtani, H. Terasaki, R. Tateyama, T. Sakamaki, T. Tsuchiya, and K.-i. Funakoshi (2011), Effect of hydrogen on the melting temperature of FeS at high pressure:

Implications for the core of Ganymede, *Earth and Planetary Science Letters*, *301*(1-2), 153–158.

Shibazaki, Y., H. Terasaki, E. Ohtani, R. Tateyama, K. Nishida, K.-i. Funakoshi, and Y. Higo (2014), High-pressure and high-temperature phase diagram for Fe0.9Ni0.1–H alloy, *Physics of the Earth and Planetary Interiors*, *228*, 192–201.

Shim, S.-H. (2017), PeakPo – A python software for X-ray diffraction analysis at high pressure and high temperature., doi:10.5281/zenodo.1193836.

Stewart, A. J., M. W. Schmidt, W. Van Westrenen, and C. Liebske (2007), Mars: A new core-crystallization regime, *Science*, *316*(5829), 1323–1325.

Strobel, T. A., P. Ganesh, M. Somayazulu, P. Kent, and R. J. Hemley (2011), Novel cooperative interactions and structural ordering in H2S-H2, *Physical review letters*, *107*(25), 255,503.

Stähler, S., S. Ceylan, A. C. Duran, R. Garcia, D. Giardini, Q. Huang, A. Khan, D. Kim, P. Lognonné, R. R. Maguire, A. G. Marusiak, A. C. Plesa, H. Samuel, N. C. Schmerr, M. Schimmel, D. Sollberger, E. Stutzmann, D. Antonangeli, J. F. Clinton, M. v. Driel, M. Drilleau, T. Gudkova, A. Horleston, J. Irving, T. Kawamura, V. Lekic, R. Myhill, F. Nimmo, M. Panning, A. Rivoldini, C. Schmelzbach, S. Stanley, R. C. Weber, Z. Xu, G. Zenhäusern, and B. W. Banerdt (2021), Seismic detection of the martian core by Insight, *52nd Lunar and Planetary Science Conference*.

Tagawa, S., K. Ohta, K. Hirose, C. Kato, and Y. Ohishi (2016), Compression of Fe–Si–H alloys to core pressures, *Geophysical Research Letters*, *43*(8), 3686–3692.

Thompson, E. C., B. A. Chidester, R. A. Fischer, G. I. Myers, D. L. Heinz, V. B. Prakapenka, and A. J. Campbell (2016), Equation of state of pyrite to 80 GPa and 2400 K, *American Mineralogist*, *101*(5), 1046–1051.

Umemoto, K., and K. Hirose (2015), Liquid iron-hydrogen alloys at outer core conditions by first-principles calculations, *Geophysical Research Letters*, *42*(18), 7513–7520.

Urakawa, S., K. Someya, H. Terasaki, T. Katsura, S. Yokoshi, K.-i. Funakoshi, W. Utsumi, Y. Katayama, Y.-i. Sueda, and T. Irifune (2004), Phase relationships and equations of state for FeS at high pressures and temperatures and implications for the internal structure of Mars, *Physics of the Earth and Planetary Interiors*, *143*, 469–479.

Usui, T., C. M. Alexander, J. Wang, J. I. Simon, and J. H. Jones (2012), Origin of water and mantle–crust interactions on Mars inferred from hydrogen isotopes and volatile element abundances of olivine-hosted melt inclusions of primitive shergottites, *357*, 119–129.

Vinet, P., J. Ferrante, J. H. Rose, and J. R. Smith (1987), Compressibility of solids, *Journal of Geophysical Research: Solid Earth*, *92*(B9), 9319–9325.

Wade, J., and B. Wood (2005), Core formation and the oxidation state of the Earth, *Earth and Planetary Science Letters*, *236*(1-2), 78–95.

Wang, Z., and H. Becker (2017), Chalcophile elements in Martian meteorites indicate low sulfur content in the Martian interior and a volatile element-depleted late veneer, *Earth and Planetary Science Letters*, *463*, 56–68.

Wänke, H., and G. Dreibus (1988), Chemical composition and accretion history of terrestrial planets, *Philosophical Transactions of the Royal Society of London. Series A, Mathematical and Physical Sciences*, *325*(1587), 545–557.

Ye, Y., V. Prakapenka, Y. Meng, and S.-H. Shim (2017), Intercomparison of the gold, platinum, and MgO pressure scales up to 140 GPa and 2500 K, *Journal of Geophysical Research: Solid Earth*, *122*(5), 3450–3464.

Yoder, C., A. Konopliv, D. Yuan, E. Standish, and W. Folkner (2003), Fluid core size of Mars from detection of the solar tide, *Science*, *300*(5617), 299–303.

Yokoo, S., K. Hirose, R. Sinmyo, and S. Tagawa (2019), Melting experiments on liquidus phase relations in the Fe-S-O ternary system under core pressures, *Geophysical research letters*, *46*(10), 5137–5145.

Yuan, L., E. Ohtani, D. Ikuta, S. Kamada, J. Tsuchiya, H. Naohisa, Y. Ohishi, and A. Suzuki (2018), Chemical reactions between Fe and H2O up to megabar pressures and implications for water storage in the Earth's mantle and core, *Geophysical Research Letters*, *45*(3), 1330–1338.

Zurkowski, C. (2020), Stability of Fe2S and phase relations in the Fe–S–O system to 170 GPa and high temperatures, *Tech. rep.*, Knowledge@ UChicago.

SM1 **Supporting Information**

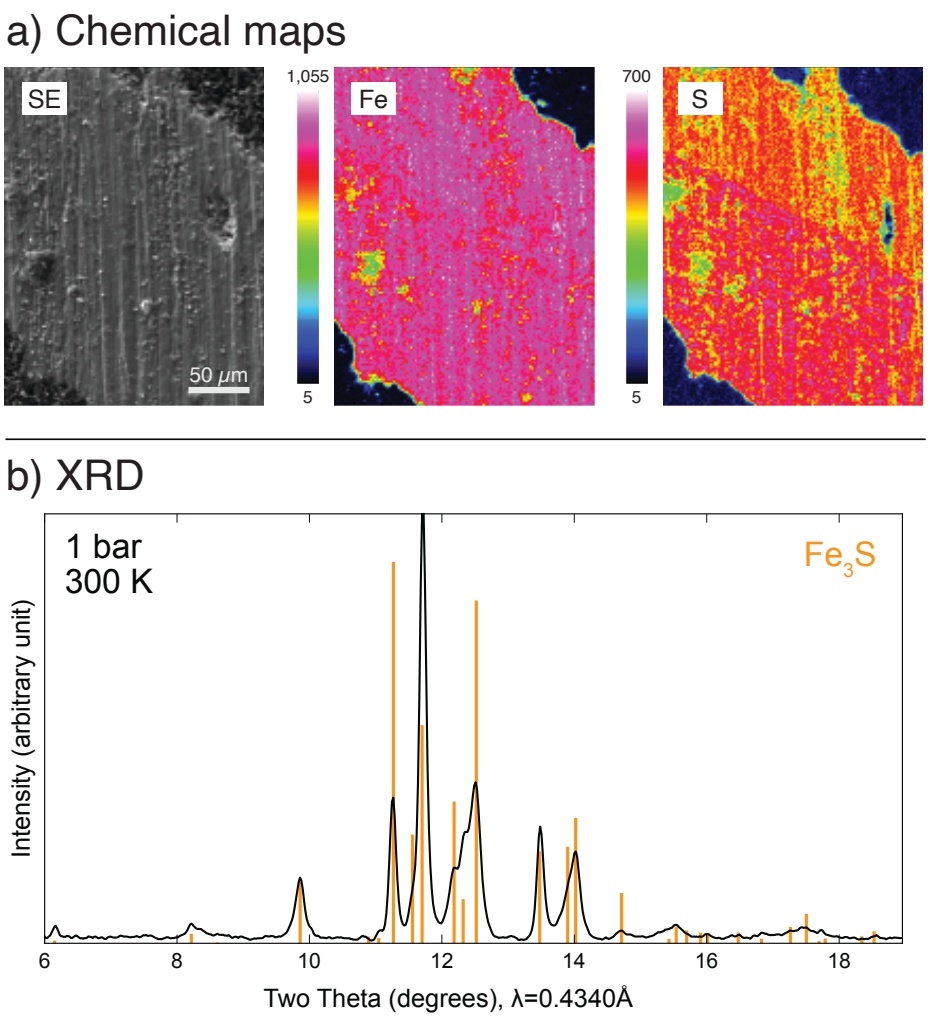

Fig. S1. Scanning electron microscopy (SEM) and X-ray diffraction (XRD) data for pure Fe_3S synthesized in the multi-anvil press. (a) Secondary electron image and corresponding iron and sulfur WDS maps showing homogeneity of the sample for both chemical elements. Some areas with different colors in the compositional maps are from surface roughness of the unpolished cross sectional areas of the multi-anvil press sample. Point analyses in those areas give similar Fe and S compositions (see Table S1. (b) XRD for this sample shows pure Fe_3S.

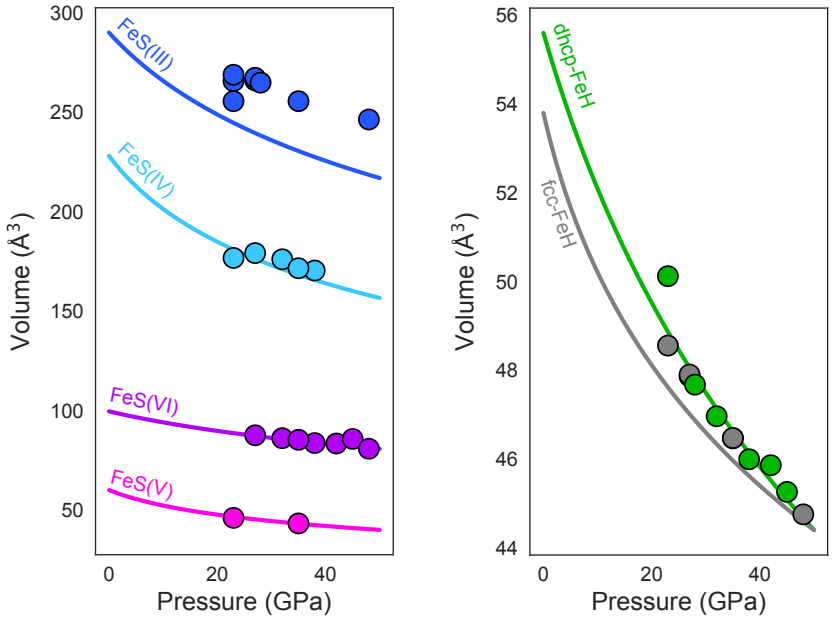

Fig. S2. The unit-cell volumes of FeS(III), FeS(IV), FeS(V) and FeS(VI) laser-heated in a H medium in this study (the colored circles). The colored lines represent equations of state of the same phases from the literature [FeS(III): *Kusaba et al.* [1997]; FeS(IV) and FeS(V): *Urakawa et al.* [2004]; FeS(VI): *Ono and Kikegawa* [2006]; dhcp-FeH: *Pépin et al.* [2014]; fcc-FeH: *Narygina et al.* [2011]]. FeS(IV) shows a slight increase and FeS(III) shows a significant increase. Such increases in the unit-cell volume suggest the presence of H in the crystal structures.

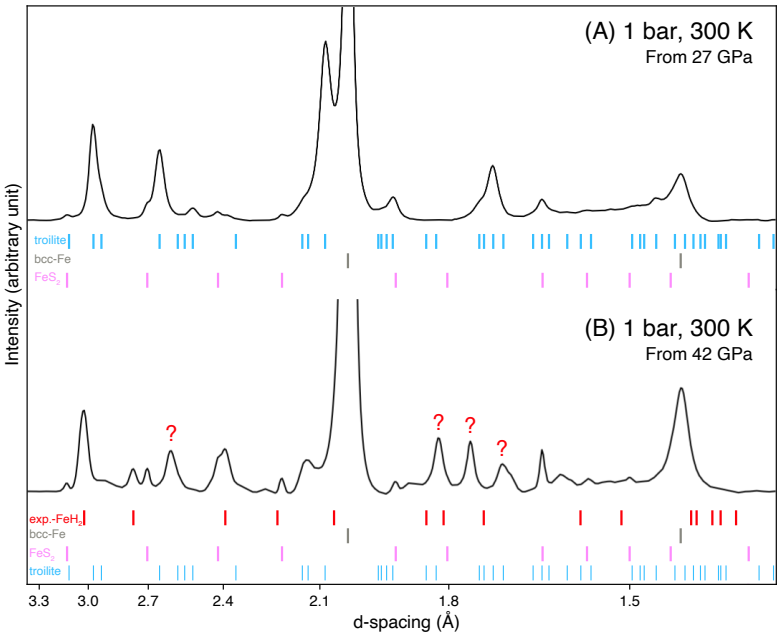

Fig. S3. XRD diffraction patterns measured at 1 bar and 300 K after decompression. A) [Fe+Fe_3S] + H_2 reacted at 27 GPa. Troilite (FeS(I)), bcc-Fe and FeS_2 are present. B) [Fe+Fe_3S] + H_2 reacted at 42 GPa. Bcc-Fe and FeS_2 are present, as well as some new diffraction lines.

Tab. S1. Electron probe micro-analysis (EPMA) quantitative point analyses for the Fe_3S starting material synthesized in the multi anvil press. Uncertainty on the measurement is shown in parentheses. The data were obtained using wavelength dispersive spectroscopy (WDS). See text for details about the samples and microprobe analysis procedure.

Sample	max. T (K)	Phases	S (wt.%)	Fe (wt.%)	Total (wt.%)
BB1520	1533	Fe_3S	14.47 (4)	84.99 (11)	99.46
		Fe_3S	16.41 (4)	83.27 (10)	99.68

Tab. S2. Experimental runs. Uncertainties on the last digit(s) are shown in parenthesis.

Run #	Starting Material	Pressure (GPa)	Temperature range (K)
231e	Fe_3S	28(2)	2820
331e	Fe_3S	32(2)	1930–2580
431e	Fe_3S	37(3)	3130–3950
120–220	Fe_3S	38(3)	1692–4057
320	Fe_3S	45(3)	2281–3076
132a	FeS	23(2)	1892–2272
103b	FeS	35(2)	1791–4579
131c	Fe-Fe_3S	27(2)	1150–2670
231c–431c	Fe-Fe_3S	42(3)	1520–4437

Tab. S3. X-ray diffraction data for the new phase (FeSH) at 38 GPa. Unit-cell volume parameters are: $a = b = 2.979(3)$ Å, $c = 10.401(13)$ Å and $\alpha = \beta = \gamma = 90°$. h, k, l are Miller indices, 2θ is the Bragg angle and d is the d-spacing. obs: observed; calc: calculated; diff: difference.

h	k	l	2θ-obs (degrees)	d-obs (Å)	d-calc (Å)	d-diff (Å)
1	0	1	6.7034	2.8599	2.8617	-0.0018
0	0	4	7.3781	2.5986	2.6017	-0.0031
1	0	3	8.4880	2.2593	2.2589	0.0004
1	1	4	11.717	1.6380	1.6363	0.0017

Tab. S4. Volume difference between hcp-Fe (baseline) and different alloys (iron hydrides and iron sulfides). The corresponding volume increase caused by one atom of H was calculated and averaged over all Fe-rich alloys. The same analysis was performed for S.

Baseline	Alloy	ΔV (Å^3/Fe)	# of H or S per Fe	ΔV/(# of S or H) (Å^3/Fe)
hcp-Fe	dhcp-FeH	1.56	1.00	1.56
	FeH_2	3.82	2.00	1.91
	FeH_3	5.86	3.00	1.95
	FeH_5	10.05	5.00	2.01
hcp-Fe	Fe_3S	2.89	0.33	8.66
	Fe_2S	4.22	0.50	8.43
	FeS	9.86	1.00	9.86
	FeS_2	21.46	2.00	10.73